# Gamma Ray Induced Formation of Uranyl Peroxide Cage Clusters

*Daniel E. Felton,[1] Melissa Fairley,[2] Ana Arteaga,[3] May Nyman,[3] Jay A. LaVerne,[2,5] Peter C. Burns[1,4]**

[1]Department of Chemistry and Biochemistry, University of Notre Dame, Notre Dame, IN 46556.
[2]Radiation Laboratory, University of Notre Dame, Notre Dame, IN 46556.
[3]Department of Chemistry, Oregon State University, Corvallis, OR, 97330.
[4]Department of Civil and Environmental Engineering and Earth Sciences, University of Notre Dame, Notre Dame, IN 46556.
[5]Department of Physics, University of Notre Dame, Notre Dame, IN 46556.
*pburns@nd.edu

**Abstract**

Aqueous solutions of lithium uranyl triperoxide, $Li_4[UO_2(O_2)_3]$ (LiUT), were irradiated with gamma rays at room temperature and found to form the uranyl peroxide cage cluster, $Li_{24}[(UO_2)(O_2)(OH)]_{24}$ (Li-$U_{24}$) . Raman spectroscopy and $^{18}O$ labeling were used to identify the Raman-active vibrations of LiUT. With these assignments the concentration of LiUT was tracked as a function of radiation dose. A discrepancy between monomer removal and cluster formation suggests that the reaction proceeds by the assembly of an intermediate. Non-negative matrix factorization was used to separate Raman spectra into components and resulted in the identification of a unique intermediate species. Much of the conversion appears to be driven by water radiolysis products, particularly the hydroxyl radical. This differs from the $^{18}O$ labeled copper catalyzed formation of $U_{24}$ which progresses at a steady rate with no observation of intermediates. Li-$U_{24}$ in solution decomposes at high radiation doses resulting in a solid insoluble product similar to Na-compreignacite, $Na_2(UO_2)_6O_4(OH)_6 \cdot 7H_2O$, which contains uranyl oxy hydroxy sheets.

## Introduction

The structures of complex macroions that spontaneously form in solution, or self-assemble, are typically studied after crystallization. One class of complex macroions are polyoxometalates (POMs) that consist of multiple metal-oxo species connected by bridging oxygen atoms yielding a finite cluster.[1,2] High oxidation state metals, such as W, Nb, Mo, and Ta form POMs because they can coordinate to multiple anions and link to doubly-bonded “yl” oxygen atoms that act as passivating ligands, stabilizing the surfaces of the clusters.[3] POMs can reach a nuclearity of up to at least 368, despite containing a small number of unique building blocks.[3,4] To better understand their solution properties, mass spectrometry is used to identify prominent species present,[2,5–8] but this provides only limited insight into formation mechanisms. The formation mechanism of POMs has been long-sought after[2,8] and recent efforts have emphasized formation kinetics of POMs and how fragments of these clusters combine to form larger species.[9,10]

Currently lacking is a detailed mechanistic understanding of the formation of actinyl peroxide cage clusters, first introduced in 2005.[11] More than 70 uranyl ($UO_2^{2+}$) peroxide clusters have been reported to date[12,13] that assemble in aqueous solution over a wide pH range and that can also contain transition metals, phosphate, and organic ligands.[12,14] Potential applications include incorporating actinides, such as plutonium, into uranyl peroxide cage clusters by ion exchange to create a precursor for mixed oxide nuclear fuels.[15] Uranyl peroxide clusters can also be used to separate actinides from fission products using a size separation via ultrafiltration[16] as well as being used as components of solid-state electrodes.[17] Recent applications of mass spectrometry and small angle X-ray scattering have led to better solution characterization of uranyl peroxide clusters and POMs, but typically do not reveal their formation pathway.[7,18,19] Knowledge of the mechanism of uranyl peroxide phase formation in a variety of conditions will aid in cluster discovery and prediction of speciation in synthetic and natural environments.

Under specific aqueous solution conditions, uranyl triperoxide monomers ($[UO_2(O_2)_3]^{4-}$, UT) assemble into uranyl peroxide clusters at room temperature.[20,21] The rate of the reaction is significantly influenced by the specific counter cation present, the pH, solvent, and the presence of uncoordinated hydrogen peroxide.[21–23] Conversion of UT in solution to the $[(UO_2)O_2OH]_{24}{}^{24-}$ ($U_{24}$) uranyl peroxide cluster, with Li counter cations, requires about a month at room temperature even at millimolar concentrations of the monomer,[20] when excess peroxide and lithium are present. The assembly reaction can be catalyzed (peroxide decomposition) by micromolar concentrations of copper that decreases reaction time to twelve hours.[22] Isolation of intermediate products during the catalyzed assembly process is challenging as the reaction, once initiated, proceeds to fully assembled clusters. An improved mechanistic understanding of the assembly process requires better control over the reaction.

Here, using the well-studied LiUT to Li-$U_{24}$ reaction as an example we examine the use of ionizing radiation to promote this reaction. Exploiting radiation energy to promote reactivity, we can pause the assembly by removing samples from the ionizing gamma radiation for characterization of reaction intermediates and determination of the cluster assembly process. The response of nanoscale metal oxide clusters to high doses of ionizing radiation is poorly explored in general, and in the case of uranyl peroxide cage clusters is important for potential applications in nuclear fuel cycles.[24] The effects of ionizing radiation on selected uranyl peroxide species have been explored in the solid state[25,26] but not in solution. Thus, the degradation of Li-$U_{24}$ in solution is also reported.

## Experimental

*Warning*: Even though depleted uranium was used in these experiments it is still radioactive and care should be taken to ensure work done does not lead to radioactive exposure. Only trained personal in approved areas should handle radioactive materials.

**Synthesis**. Solid lithium uranyl triperoxide (LiUT) [$Li_4(UO_2)(O_2)_3 \cdot 10H_2O$] was synthesized according to previously reported methods (See supporting information).[22,24,27] Crystals of LiUT were collected using vacuum filtration, dried, and stored at 4°C. The polycrystalline LiUT was analyzed using powder X-ray diffraction (Figure S1), inductively coupled plasma optical emission spectrometry, electrospray ionization mass spectrometry, and Raman spectroscopy to characterize purity. Isotopic labeling of uranyl nitrate hexahydrate with $^{18}O$ was done according to a reported procedure[28] using 97% $H_2{}^{18}O$ (Cambridge Isotope Laboratories, Inc.). The labeled uranyl nitrate was then used to make $^{18}O$-yl labeled LiUT.

The Li analog of compreignacite was synthesized through modification of a reported synthesis for compreignacite [$K_2(UO_2)_6O_4(OH)_6 \cdot 7H_2O$].[29] A 5 mL aqueous solution containing 0.21g of uranyl acetate dihydrate and 0.1 g of lithium chloride (≥99%, Macron Fine Chemicals) was placed in a 23 mL Parr reaction vessel in a Teflon liner and heated in an oven at 100°C for 24 h. The yellow powder was collected by vacuum filtration and was washed with deionized water.

**Irradiation**. Gamma irradiations were performed using an enclosed Shepherd $^{60}Co$ source at the University of Notre Dame. The dose rate was determined via Fricke dosimetry to be approximately 89 Gy/min and has been corrected for decay since calibration. Solutions of 50 mg/mL (~0.1M) LiUT, produced by dissolving LiUT in ultrapure water, were flame-sealed in Pyrex tubes (1 cm diameter by 10 cm long) that were either under ambient conditions, purged with nitrous oxide, or purged with argon prior to irradiation. Control samples were prepared using the same method but were then left on the benchtop for the duration of the irradiation experiment to ensure no temporal changes occurred. No significant changes were seen in the Raman spectra collected for the control samples over the timeframe of the radiation experiments (Figure S2). Irradiation in the $^{60}$Co source causes samples to heat slightly. To determine the effect of heat on samples, solutions were sealed under atmospheric conditions and heated to 30°C in an oven (Figure S3, S4, and supporting information for more details). No effects due to heating were observed in the irradiated samples.

**Raman Spectroscopy.** Raman spectra were collected using a Renishaw inVia spectrometer. A 785 nm 300 mW laser with a spot size of 30 µm was used for all measurements. A mirror was used to direct the laser 90° to a cuvette holder that ensured the cuvette was the same distance from the lens for each measurement (Figure S5). The sample tubes were broken open and the liquid, along with suspended precipitate, was transferred to a centrifuge tube to separate the solid and liquid. The liquid was transferred to a glass cuvette for spectral measurement. Static scans were taken using a laser power of 100%, 10 second scans, and 12 accumulations for all solutions. Cosmic ray removal was used for all spectra. Peaks were background subtracted using a Sonneveld and Visser fitting[30] then fit using a Lorentzian/Gaussian function, all in Matlab.[31]

**Electrospray ionization mass spectrometry (ESI-MS)**. Spectra were collected using a Bruker QTOF Compact LC-MS high-resolution mass spectrometer in the negative ion mode with 3700 V capillary voltage, endplate offset of -500 V, 0.8 bar nebulizer gas, 4.0 L/min dry gas, and 180°C dry gas temperature. Solutions were diluted with ultrapure water to uranium concentrations of less than 100 ppm. Spectra were collected and averaged over a 5-minute period.

**Small Angle X-ray Scattering (SAXS).** Solution scattering was recorded using a Bruker NANOSTAR SAXS. Solutions were placed in 1.5 mm capillary tubes and the ends were sealed with vacuum resistant glue. Data was collected for one hour per sample with a Cu K$\alpha$ microfocus source at 45kV and 650μA. Backgrounds were collected using the same capillaries containing ultra-pure water. Data was collected with DIFFRAC.SAXS and preliminary processing, such as, background subtraction, integration, and Guinier analysis were also performed. The IRENA[32] package for IGOR Pro was used to fit the data with a core-shell model to give the radius of gyration reported. The scattering curve of $U_{24}$ was calculated using single crystal data in SolX.[33]

**Inductively coupled plasma optical emission spectroscopy (ICP-OES)**. Chemical analyses were performed using a PerkinElmer Avio 200 ICP-OES. Data were collected using 1400 μW power, 8 μL/min plasma flow rate, and a 0.6 L/min nebulizer flow rate. Prior to analysis compounds were dissolved in 2% nitric acid and diluted to appropriate concentrations of each analyte. Matrix matched standards and internal standards were used to calibrate and monitor for instrument drift. Molar ratios of U and Li were calculated from the results with an analytical uncertainty of ~3.5%. Experimental molar ratio (Li:U) of the degradation product (1:1.127)

**Powder X-Ray Diffraction (PXRD)**. Patterns were collected using a Bruker D8 Advance Davinci powder X-ray diffractometer equipped with a Cu $K_\alpha$ X-ray source. Scans were collected from 5-50° 2θ, with 0.04° scan step, and 1 second per step while the sample was rotated at 15 rpm about phi.

**Gas Chromatography (GC).** Data was collected using a SRI 8610 gas chromatograph with a 3 m molecular sieve column and helium carrier gas. Samples were sealed under vacuum to exclude oxygen from the atmosphere. If signals corresponding to nitrogen were observed a correction was made to remove the appropriate amount of oxygen at the end of the calculation. Calibration was done by injecting a known amount of air into the GC.

## Results and Discussion

Conversion of UT to $U_{24}$ in aqueous solution as a function of ionizing radiation dose was monitored by *ex situ* Raman spectroscopy as uranyl and peroxide both yield strong Raman bands.[34] The Raman bands of UT and $U_{24}$ overlap at 815 $cm^{-1}$ but a band at 715 $cm^{-1}$ is unique to UT (**Figure 1**). Previous assignments of these uranyl triperoxide bands to vibration modes are not in agreement.[22,35,36] Thus, the vibrational assignments were investigated using isotopic labeling.

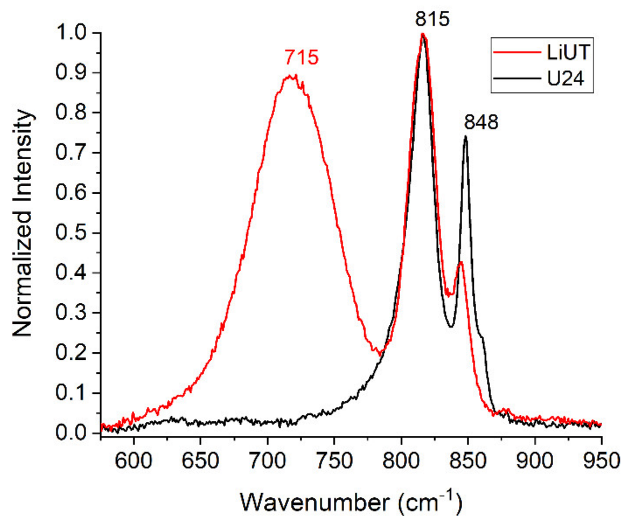


***Figure 1**. Raman spectra of lithium uranyl triperoxide (LiUT) and $Li_{24}[(UO_2)O_2OH]_{24}$ ($LiU_{24}$). Spectra are normalized to 1. The 715 $cm^{-1}$ peak is unique to LiUT and can be used to track concentration in solution.*

The self-assembly of isotopically labelled uranyl ions into $U_{24}$ was studied using an approach similar to that of Dembowski et al.[36] A solution of LiUT in which the oxygen atoms of the linear uranyl ($UO_2^{2+}$) ion were labelled with $^{18}O$ ($^{18}O$-yl) was reacted with $Cu^{2+}$ to catalyze UT assembly into $U_{24}$. The reaction was monitored *in-situ* by Raman spectroscopy every thirty minutes (Figure S6). The $^{18}O$ label was lost due to proton exchange between the axial uranyl oxygen atoms and equatorial hydroxide under basic conditions,[37] so the experiment was repeated with $H_2{}^{18}O$ and the $^{18}O$ label was retained (**Figure 2**). The solution containing $^{18}O$-yl UT (Figure 2, '0 Hours') produces a Raman peak at 686 $cm^{-1}$ instead of 715 $cm^{-1}$ for the unlabeled material, with this red-shift indicating that the peak corresponds purely to the uranyl symmetric vibration of UT.

Similarly, the spectrum of $U_{24}$ with $^{18}O$ labeled uranyl (Figure 2, 10 Hours) has a peak at 774 $cm^{-1}$ instead of 815 $cm^{-1}$ for the unlabeled material, corresponding to the uranyl symmetric vibration of the cluster. In the spectra of nonlabelled $U_{24}$ (**Figure 1**), there is a slight shoulder at 860 $cm^{-1}$ that becomes much less pronounced in the spectra of labelled $U_{24}$ and the peak at 848 $cm^{-1}$ is much more intense. This change is most likely due to a shift of the bridging hydroxyl between uranyl ions that is present in $U_{24}$ but definite assignment is beyond the scope of this paper. These shifts are in agreement with previous labeling studies done on uranyl peroxides.[36,38] The assembly reaction proceeds directly from monomer to cluster as shown by the isosbestic point just under 800 $cm^{-1}$ in **Figure 2** and does so at a consistent rate as seen by the uniformly changing intensities of the bands over time.

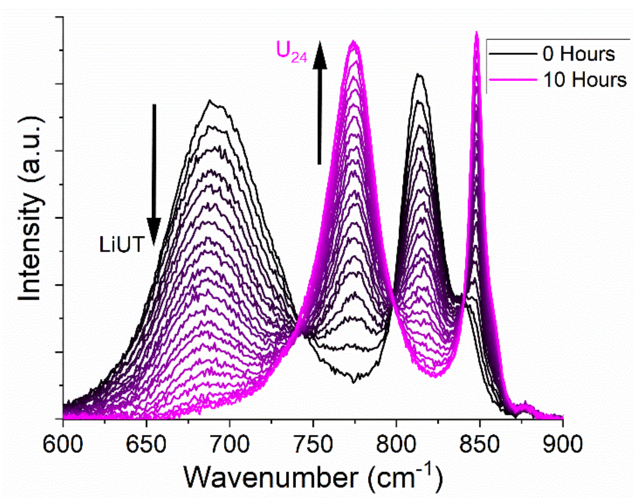


***Figure 2.*** *Conversion of lithium uranyl triperoxide (LiUT) to $Li_{24}[(UO_2)O_2OH]_{24}$ (Li$U_{24}$) with $^{18}O$ labeled uranyl ($UO_2^{2+}$) performed in $H_2{}^{18}O$ over time.*

With a better understanding of the assignments of the Raman bands produced by solutions of UT and $U_{24}$ revealed by isotopic labelling studies in hand, the concentration of the UT monomer can be monitored using the intensity of the 715 $cm^{-1}$ peak during irradiation studies. The Raman spectra for samples of irradiated UT solutions are shown in **Figure 3**a. The intensity of the peak at 715 $cm^{-1}$ does not uniformly decrease with increasing radiation dose as was observed in the Cu-catalyzed $^{18}O$ labeling experiment (**Figure 2**). Additionally, there is a delay in the increase of the intensity of the 848 $cm^{-1}$ peak that is correlated to $U_{24}$ formation.

A peak fit of the LiUT uranyl vibration (715 $cm^{-1}$) was used to derive the concentration of the monomer as a function of radiation dose as shown in **Figure 3**b. The initial rate of decay of

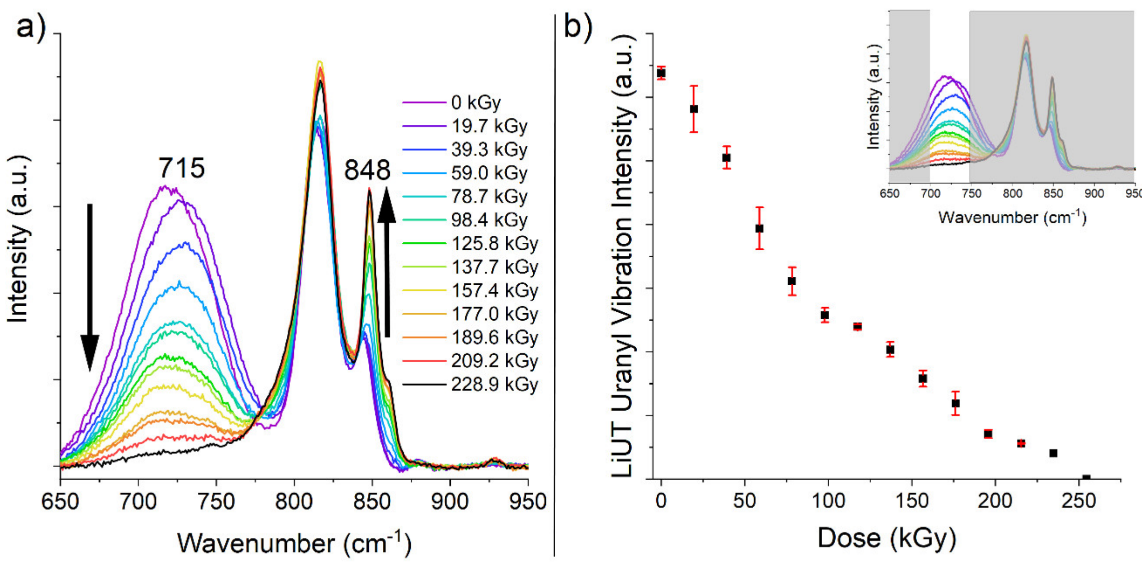


*__Figure 3.__ a) Raman spectra of lithium uranyl triperoxide (LiUT) converting to $Li_{24}[(UO_2)O_2OH]_{24}$ (LiU24) with increasing dose. The peak at 715 $cm^{-1}$ is unique to LiUT and can be used to track concentration in solution. b) Plot of lithium uranyl triperoxide (LiUT) concentration with respect to dose. Error bars are shown in red and represent standard deviation.*

UT is faster than it is subsequent to ~80 kGy, and the intensity of the 848 $cm^{-1}$ peak is almost constant at doses below ~80 kGy. This dose dependence indicates that monomer is not immediately converting to $U_{24}$ as it was with our $^{18}O$ Cu-catalyzed reaction. This delay is consistent with the formation of a fragment of $U_{24}$ such as the theorized uranyl peroxide tetramer, $Li_8[UO_2(O_2)OH_2]_4$, shown in **Scheme 1**.[22,39,40]

To better interpret the Raman spectra a non-negative matrix factorization (NMF) algorithm[41] was used to separate each spectrum into a sum of components as seen in **Figure 4**a. The first and third components match the spectra of LiUT and Li-$U_{24}$ respectively. The second component resembles that of LiUT but instead has a band shifted from the 715 $cm^{-1}$ of LiUT to 743 $cm^{-1}$. A similar shift was seen when a solution of potassium uranyl triperoxide formed a building block of uranyl peroxide cage clusters, $K_{10}[(UO_2)_5(O_2)_{10}]$, in solution.[23] This would suggest component two is an intermediate that exists in solution for an extended period of time (hours) before converting to $U_{24}$. This would also explain why the Raman peak at 715 $cm^{-1}$ seems to shift to higher wavenumbers as seen in the spectra of the '19.7kGy' solution (**Figure 3**a). Instead of being one peak it is the sum of two peaks, causing the appearance of a peak shift where one does not exist. Uranyl Raman bands of solutions can shift due to changes in pH but the supposed shift to higher wavenumbers observed in Figure 3a would correspond to a decrease in pH (Figures S7 and S8) which is not the case. Figure 4b shows the relative amounts of each component in solution as a function of dose. The intermediate forms quickly with a low dose but as a higher dose is given, we see more and more Li-$U_{24}$ in solution.

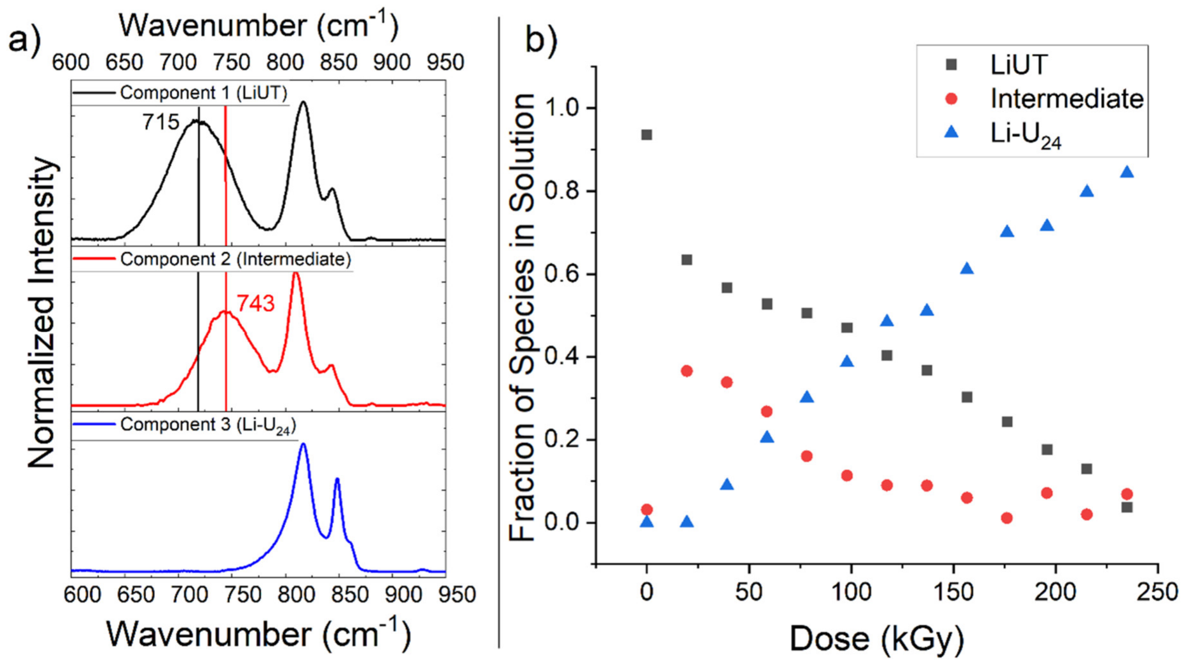


***Figure 4.*** *a) Components of the Raman spectra from **Figure 3**a from a non-negative matrix factorization. Vertical lines show the shift in the broad peak between components 1 and 2. b) The relative amount of each component from **Figure 4**a contained in each Raman spectrum from **Figure 3**a. There is a fourth component that omitted here for clarity (Figure S ). Residuals for the fitting are shown in the supporting information.*

When a peroxide bridge is formed between two uranyl ions in solution, lithium hydroxide is formed, making the solution more basic (Scheme 1). The pH was measured at each dose point and was found to increase steadily up to a dose of 40 kGy where the pH levels off around 12.85 (Figure S9). The formation of the tetramer of uranyl ions produces four hydroxide ions for each LiUT monomer consumed, explaining the sharp increase in pH at low doses (Scheme 1). It also correlates well to the NMF component analysis as there is a sharp increase of the intermediate at low dose which in turn increases the pH. There are multiple ways to balance the equation in Scheme 1, such as by having the terminal peroxides of LiUT dissociate instead of disproportionate leading to 'free' peroxide in solution. A Raman peak seen at 875 cm$^{-1}$ corresponding to hydrogen peroxide can be seen until 80 kGy implying the peroxide is dissociating up to this dose with disproportionation then being favored after 80 kGy.

Another way to balance the formula in Scheme 1 would be for the tetramer to have a terminal peroxide instead of two hydroxides per uranyl. This would result in half as much hydroxide and oxygen gas formation per mole of LiUT. GC measurements were performed to record oxygen production and determine which scheme was correct. Solutions of LiUT were irradiated to 80 kGy, when approximately half of the LiUT in solution is depleted and free peroxide is no longer observed in the Raman. We would expect to measure ~0.5 moles of oxygen gas per mole of LiUT at this dose. Measurements gave an $O_2$(g)/LiUT molar ratio of 0.546 ± .034 indicating that terminal hydroxides are favored over terminal peroxides during intermediate formation.

***Scheme 1.*** *Reaction of lithium uranyl triperoxide with water to form a uranyl peroxide hydroxide tetramer, lithium hydroxide, and oxygen gas. The reaction can be balanced using oxygen radicals such as hydroperoxyl instead of water, but this emphasizes the formation of lithium hydroxide when a peroxide bridge is formed between two uranyl ions.*

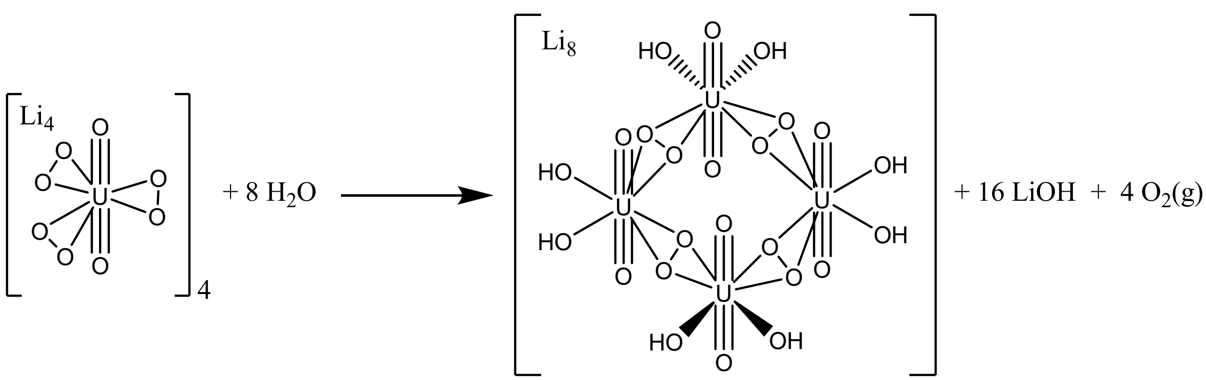


To better understand the effect of pH, a solution of LiUT was irradiated to 65 kGy, after which the pH was increased by adding 4M lithium hydroxide dropwise (Figure S10). The Raman peak at 715 $cm^{-1}$ corresponding to the uranyl vibration of UT increased in intensity following addition of lithium hydroxide but the peak at 845 $cm^{-1}$, corresponding to $U_{24}$ formation, did not change. The intensity of the Raman peak at 875 $cm^{-1}$ assigned to hydrogen peroxide also increases upon addition of LiOH, suggesting that the terminal peroxide of LiUT and tetramers exist in an equilibrium with hydroxide in solution. However, after 80 kGy of irradiation, when no Raman mode corresponding to hydrogen peroxide in solution is observed, the excess hydroxide and low peroxide concentration causes $U_{24}$ formation to be favored.

To assess the impact of these radicals on the conversion rate of UT to $U_{24}$, a LiUT solution was purged with argon and a second was purged with nitrous oxide prior to irradiation. During irradiation, energy is deposited in the entire system, the vast majority of which is absorbed by water, producing reactive species that induce decomposition of LiUT. This process, termed water radiolysis, produces various species, most prominent of which are reducing hydrated electrons and oxidizing hydroxyl radicals. The argon purge removes oxygen gas that would react with solvated electrons formed during gamma irradiation, a precursor to the hydroxide radical. The nitrous oxide purge also removes oxygen gas prior to irradiation but goes further by reacting with the solvated electrons to form a stoichiometric amount of hydroxyl radicals, increasing the radical concentration further than for argon.[42] These samples were then irradiated side-by-side to 58.7 kGy and Raman spectra were taken for each solution. Compared to the spectrum of the irradiated solution that was sealed under an ambient atmosphere, less LiUT was observed for the sample purged with argon, and even less so for the solution purged with $N_2O$ (Figure S11). These results indicate that hydroxyl radicals are the main radiolysis product inducing the decomposition of LiUT. Presumably, they react with the terminal peroxide of LiUT to enhance production of the tetramer intermediate.

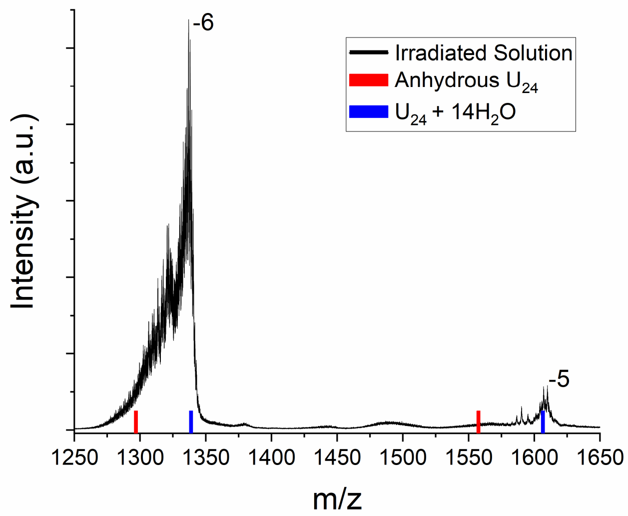


***Figure 5.*** *Mass spectra of a solution of lithium uranyl triperoxide (LiUT) irradiated to ~235 kGy showing the presence of $Li_{24}[(UO_2)O_2OH]_{24}$ ($LiU_{24}$) clusters. The red bars are simulated masses for anhydrous $LiU_{24}$ ($(Li_{18}[(UO_2)O_2OH]_{24})^{6-}$ and $(Li_{19}[(UO_2)O_2OH]_{24})^{5-}$. The blue bars are simulated masses for $LiU_{24}$ with an additional fourteen coordinated water molecules.*

ESI-MS and SAXS were used to further characterize speciation for each irradiated solution. No signals in the ESI-MS data corresponding to $U_{24}$ were observed for solutions irradiated to less than 80 kGy of gamma. We then attempted to pre-concentrate clusters using centrifugation and a 3k Dalton mass filter, but again no clusters were detected. Solutions irradiated to ~80 kGy produced ESI-MS spectra indicating the presence of $U_{24}$, and at higher doses it is a dominant species. The simulated isotopic distribution was compared to the experimental data (~235KGy) and was found to match well (Figure S12). The mass spectra are consistent with the simulated anhydrous Li-$U_{24}$ cluster and previously reported Li-$U_{24}$ structure containing fourteen water molecules within the cluster (Figure 5).[43] SAXS was collected for a sample irradiated to ~235 kGy, when the Li-$U_{24}$ concentration is highest (**Figure 6**). Using a core-shell model to fit the data gives a radius of gyration of 5.54 Å which is slightly smaller than the expected 6.6 Å.[18] This smaller radius of gyration is likely due to the subsequent breakdown of Li-$U_{24}$.

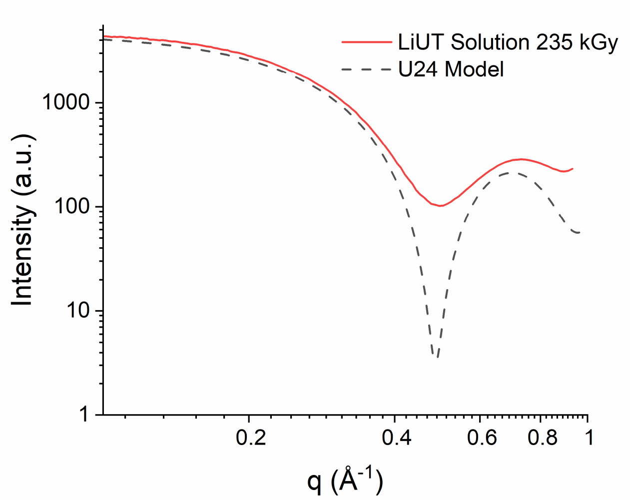


***Figure 6.*** *Small angle X-ray scattering plot of a solution of lithium uranyl triperoxide (LiUT) given a dose of 235 kGy in red and the simulated pattern for $U_{24}$. Using a core-shell model to fit the data gives a radius of gyration of 5.54 Å.*

Solutions were then monitored past 250 kGy, when no monomer signal is detected in the Raman spectrum (**Figure 3**b) to 400 kGy, when nearly all uranium has precipitated from solution. The Raman spectrum of a LiUT solution irradiated to 288 kGy exhibits a shoulder at ~780 cm$^{-1}$ (Figure S13). After a 400 kGy dose when nearly all uranium is in a precipitate, designated the degradation product henceforth, the solid was collected and dryed for analysis. The PXRD pattern of the microcrystalline degradation product was found to be similar to the reported diffractogram of Na-compreignacite, $Na_2(UO_2)_6O_4(OH)_6 \cdot 7H_2O$ (Figure S14). Na-compreignacite contains anionic sheets of uranyl pentagonal bipyramids with Na and water in the interlayer. Compounds with a similar structure, termed uranyl oxyhydroxide sheets, can be synthesized with other cations in the interlayer such as potassium and lead, but a lithium analogue has not yet been reported. The reported synthesis of Na-compreignacite[29] was altered to synthesize a Li-compreignacite solid to determine if this was indeed the identity of the degradation product. The diffraction pattern obtained from the synthetic 'Li-compreignacite' phase is similar to that of the Na-compreignacite but the degradation product from the irradiated LiUT differs from both (**Figure 7**).

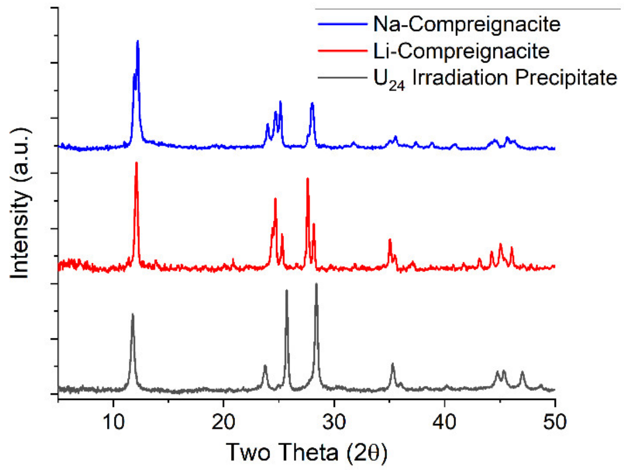


***Figure 7.*** *Powder X-ray diffraction pattern of synthetic sodium and lithium compreignacite and the precipitate that forms from irradiated $Li_{24}[(UO_2)O_2OH]_{24}$ ($LiU_{24}$) solutions.*

Analysis (ICP-OES) of the irradiation precipitate yielded a U:Li molar ratio of 1:1 rather than the expected 3:1 of a Li-substituted compreignacite, further differentiating the degradation from reported structures. This ratio indicates that there are more oxides in the sheet than hydroxides giving a formula more similar to the mineral spriggite, $Pb_3(UO_2)_6O_8(OH)_2 \cdot 3H_2O$, where the three 2+ lead ions would be replaced by six 1+ lithium ions. Numerous uranyl oxyhydroxide hydrates with anionic and neutral sheets of uranyl bipyramids have been reported that differ in their distributions of oxo and hydroxyl at equatorial positions of the bipyramids, giving the sheets different overall charges.[44,45] As such, we propose that the precipitate formed during irradiation is a lithium uranyl oxide hydroxide hydrate with a structure that is similar, but not identical, to that of the Li analog of compreignacite.

It is possible that the precipitate formed during irradiation is a dehydrated Li-compreignacite causing a further shift in X-ray diffraction peaks as seen for schoepite and its dehydrated forms.[46] Regardless of definite assignment, the d-spacing of the strongest reflection (001) of the precipitate indicates that the layer repeat is 7.44 Å. There are dozens of unique uranyl oxide hydroxy-hydrate sheet structures,[47] but results suggest that it most likely has the α-$U_3O_8$ sheet topology.

## Conclusion

In this work the uranyl peroxide cage cluster Li-$U_{24}$ was synthesized from an aqueous solution of lithium uranyl triperoxide under ionizing radiation. Radiation was shown to promote the formation of the cage cluster through reaction with hydroxyl radicals formed via water radiolysis. The aqueous Li-$U_{24}$ cluster decomposes when further exposed to gamma irradiation forming a uranyl hydroxide oxide hydrate similar to that of compreignacite. This study demonstrates that ionizing radiation can be used as a tool to promote formation of uranyl peroxide clusters and materials via mechanisms that differ from purely chemical methods. Future work needs to be done to identify the structure of the lithium uranyl hydroxide oxide hydrate. Varying the counter cation and equatorial ligands of the clusters would also allow further insight into how ionizing radiation can diversify and broaden this family of materials.

ASSOCIATED CONTENT

Supporting Information available: Details of synthesis, X-ray powder diffraction patterns of recovered solids, details of Raman experiments, Raman spectra of solutions containing LiUT prior to and following irradiation, Raman spectra of $^{18}O$-labelled systems, electrospray ionization mass spectrometry data and interpretation, measured solution pH as a function of radiation dose.

## AUTHOR INFORMATION

Corresponding Author

***Peter Burns** - *Department of Chemistry and Biochemistry, University of Notre Dame, Notre Dame, Indiana 46556, United States; Department of Civil & Environmental Engineering & Earth Sciences, University of Notre Dame, Notre Dame, Indiana 46556, USA;* orcid.org/0000-0002-2319-9628; Email: pburns@nd.edu

Authors

**Daniel E. Felton** – *Department of Chemistry and Biochemistry, University of Notre Dame, Notre Dame, Indiana 46556, USA*; orcid.org/0000-0003-0508-2466

**Melissa Fairley** – *Materials Physics and Applications Division, Los Alamos National Laboratory, Los Alamos, New Mexico 87545, USA* ; orcid.org/0000-0001-6031-7112

**Jay A. LaVerne –** *Radiation Laboratory, University of Notre Dame, Notre Dame, IN 46556*: orcid.org/0000-0002-8383-7476

**Ana Arteaga** - *Pacific Northwest National Laboratory, 902 Battelle Boulevard, Richland, WA 99354, United States, USA*; orcid.org/0000-0002-8330-2279

**May Nyman** − *Department of Chemistry, Oregon State University, Corvallis, Oregon 97331, USA*; orcid.org/0000-0002-1787-0518

## Acknowledgments

This research was supported by the Department of Energy, National Nuclear Security Administration, under Award Number DE-NA0003763 until December 2020, then by University funds. The authors acknowledge the Center for Sustainable Energy at Notre Dame (ND Energy) Materials Characterization Facility for the use of the Bruker D8 Advance Davinci powder X-ray diffractometer and NRS-5100 Jasco confocal Raman microscope. The authors thank Prof. Michael Wiescher for making available the facilities of the Notre Dame Nuclear Science Laboratory, which is supported by the U.S. National Science Foundation through Grant Phys-0758100, and Prof. Ian Carmichael for making available the facilities of the Notre Dame Radiation Laboratory, which is supported by DOE BES through Grant DE-FC02-04ER15533. This contribution is NDRL-5352 from the Notre Dame Radiation Laboratory.

## References

(1) Long, D.-L.; Burkholder, E.; Cronin, L. Polyoxometalate Clusters, Nanostructures and Materials: From Self Assembly to Designer Materials and Devices. *Chem. Soc. Rev.* **2006**, *36* (1), 105–121. https://doi.org/10.1039/B502666K.

(2) Pope, M. T.; Müller, A. Polyoxometalate Chemistry: An Old Field with New Dimensions in Several Disciplines. *Angew. Chem. Int. Ed. Engl.* **1991**, *30* (1), 34–48. https://doi.org/10.1002/anie.199100341.

(3) Nyman, M.; Burns, P. C. A Comprehensive Comparison of Transition-Metal and Actinyl Polyoxometalates. *Chem. Soc. Rev.* **2012**, *41* (22), 7354–7367. https://doi.org/10.1039/C2CS35136F.
(4) Müller, A.; Beckmann, E.; Bögge, H.; Schmidtmann, M.; Dress, A. Inorganic Chemistry Goes Protein Size: A $Mo_{368}$ Nano-Hedgehog Initiating Nanochemistry by Symmetry Breaking. *Angew. Chem. Int. Ed.* **2002**, *41* (7), 1162–1167. https://doi.org/10.1002/1521-3773(20020402)41:7<1162::AID-ANIE1162>3.0.CO;2-8.
(5) Pradeep, C. P.; Li, F.-Y.; Lydon, C.; Miras, H. N.; Long, D.-L.; Xu, L.; Cronin, L. Design and Synthesis of "Dumb-Bell" and "Triangular" Inorganic-Organic Hybrid Nanopolyoxometalate Clusters and Their Characterisation through ESI-MS Analyses. *Chem. Eur. J.* **2011**, *17* (27), 7472–7479. https://doi.org/10.1002/chem.201100257.
(6) Warzok, U.; Mahnke, L. K.; Bensch, W. Soluble Hetero-Polyoxovanadates and Their Solution Chemistry Analyzed by Electrospray Ionization Mass Spectrometry. *Chem. Eur. J.* **2019**, *25* (6), 1405–1419. https://doi.org/10.1002/chem.201803291.
(7) Robbins, P. J.; Surman, A. J.; Thiel, J.; Long, D.-L.; Cronin, L. Use of Ion-Mobility Mass Spectrometry (IMS-MS) to Map Polyoxometalate Keplerate Clusters and Their Supramolecular Assemblies. *Chem. Commun.* **2013**, *49* (19), 1909–1911. https://doi.org/10.1039/C3CC38615E.
(8) Long, D.-L.; Tsunashima, R.; Cronin, L. Polyoxometalates: Building Blocks for Functional Nanoscale Systems. *Angew. Chem. Int. Ed.* **2010**, *49* (10), 1736–1758. https://doi.org/10.1002/anie.200902483.
(9) Miras, H. N.; Mathis, C.; Xuan, W.; Long, D.-L.; Pow, R.; Cronin, L. Spontaneous Formation of Autocatalytic Sets with Self-Replicating Inorganic Metal Oxide Clusters. *Proc. Natl. Acad. Sci. USA* **2020**, *117* (20), 10699–10705. https://doi.org/10.1073/pnas.1921536117.
(10) Xuan, W.; Pow, R.; Zheng, Q.; Watfa, N.; Long, D.-L.; Cronin, L. Ligand-Directed Template Assembly for the Construction of Gigantic Molybdenum Blue Wheels. *Angew. Chem.* **2019**, *131* (32), 10983–10988. https://doi.org/10.1002/ange.201901818.
(11) Burns, P. C.; Kubatko, K.-A.; Sigmon, G.; Fryer, B. J.; Gagnon, J. E.; Antonio, M. R.; Soderholm, L. Actinyl Peroxide Nanospheres. *Angew. Chem. Int. Ed.* **2005**, *44* (14), 2135–2139. https://doi.org/10.1002/anie.200462445.
(12) Burns, P. C.; Nyman, M. Captivation with Encapsulation: A Dozen Years of Exploring Uranyl Peroxide Capsules. *Dalton Trans.* **2018**, *47* (17), 5916–5927. https://doi.org/10.1039/C7DT04245K.
(13) Qiu, J.; Burns, P. C. Clusters of Actinides with Oxide, Peroxide, or Hydroxide Bridges. *Chem. Rev.* **2013**, *113* (2), 1097–1120. https://doi.org/10.1021/cr300159x.
(14) Qiu, J.; Dong, S.; Szymanowski, J. E. S.; Dobrowolska, M.; Burns, P. C. Uranyl-Peroxide Clusters Incorporating Iron Trimers and Bridging by Bisphosphonate- and Carboxylate-Containing Ligands. *Inorg. Chem.* **2017**, *56* (7), 3738–3741. https://doi.org/10.1021/acs.inorgchem.7b00389.
(15) Blanchard, F.; Ellart, M.; Rivenet, M.; Vigier, N.; Hablot, I.; Morel, B.; Grandjean, S.; Abraham, F. Neodymium Uranyl Peroxide Synthesis by Ion Exchange on Ammonium Uranyl Peroxide Nanoclusters. *Chem. Commun.* **2016**, *52* (20), 3947–3950. https://doi.org/10.1039/C5CC09527A.
(16) Wylie, E. M.; Peruski, K. M.; Prizio, S. E.; Bridges, A. N. A.; Rudisill, T. S.; Hobbs, D. T.; Phillip, W. A.; Burns, P. C. Processing Used Nuclear Fuel with Nanoscale Control of

Uranium and Ultrafiltration. *J. Nucl. Mater.* **2016**, *473*, 125–130. https://doi.org/10.1016/j.jnucmat.2016.02.013.
(17) Hu, J.; Cai, L.; Wang, H.; Chen, K.; Yin, P. Uranyl Peroxide Nanocage Assemblies for Solid-State Electrolytes. *ACS Appl. Nano Mater.* **2021**. https://doi.org/10.1021/acsanm.1c00130.
(18) Nyman, M. Small-Angle X-Ray Scattering to Determine Solution Speciation of Metal-Oxo Clusters. *Coord. Chem. Rev.* **2017**, *352*, 461–472. https://doi.org/10.1016/j.ccr.2016.11.014.
(19) Lobeck, H. L.; Isner, J. K.; Burns, P. C. Transformation of Uranyl Peroxide Studtite, $[(UO)(O_2)(H_2O)_2](H_2O)_2$, to Soluble Nanoscale Cage Clusters. *Inorg. Chem.* **2019**. https://doi.org/10.1021/acs.inorgchem.9b00230.
(20) Falaise, C.; Nyman, M. The Key Role of $U_{28}$ in the Aqueous Self-Assembly of Uranyl Peroxide Nanocages. *Chem. Eur. J.* **2016**, *22* (41), 14678–14687. https://doi.org/10.1002/chem.201602130.
(21) Arteaga, A.; Zhang, L.; Hickam, S.; Dembowski, M.; Burns, P. C.; Nyman, M. Uranyl–Peroxide Capsule Self-Assembly in Slow Motion. *Chem. Eur. J.* **2019**, *25* (24), 6087–6091. https://doi.org/10.1002/chem.201806227.
(22) Liao, Z.; Deb, T.; Nyman, M. Elucidating Self-Assembly Mechanisms of Uranyl–Peroxide Capsules from Monomers. *Inorg. Chem.* **2014**, *53* (19), 10506–10513. https://doi.org/10.1021/ic501587g.
(23) Arteaga, A.; Ray, D.; Glass, E.; Martin, N. P.; Zakharov, L. N.; Gagliardi, L.; Nyman, M. The Role of the Organic Solvent Polarity in Isolating Uranyl Peroxide Capsule Fragments. *Inorg. Chem.* **2020**, *59* (3), 1633–1641. https://doi.org/10.1021/acs.inorgchem.9b02660.
(24) Armstrong, C. R.; Nyman, M.; Shvareva, T.; Sigmon, G. E.; Burns, P. C.; Navrotsky, A. Uranyl Peroxide Enhanced Nuclear Fuel Corrosion in Seawater. *Proc. Natl. Acad. Sci. USA* **2012**, *109* (6), 1874–1877. https://doi.org/10.1073/pnas.1119758109.
(25) Fairley, M.; Myers, N. M.; Szymanowski, J. E. S.; Sigmon, G. E.; Burns, P. C.; LaVerne, J. A. Stability of Solid Uranyl Peroxides under Irradiation. *Inorg. Chem.* **2019**. https://doi.org/10.1021/acs.inorgchem.9b02132.
(26) Fairley, M.; Felton, D. E.; Sigmon, G. E.; Szymanowski, J. E. S.; Poole, N. A.; Nyman, M.; Burns, P. C.; LaVerne, J. A. Radiation-Induced Solid-State Transformations of Uranyl Peroxides. *Inorg. Chem.* **2022**, *61* (2), 882–889. https://doi.org/10.1021/acs.inorgchem.1c02603.
(27) Nyman, M.; Rodriguez, M. A.; Campana, C. F. Self-Assembly of Alkali-Uranyl-Peroxide Clusters. *Inorg. Chem.* **2010**, *49* (17), 7748–7755. https://doi.org/10.1021/ic1005192.
(28) Gaziev, S. A.; Gorshkov, N. G.; Mashirov, L. G.; Suglobov, D. N. Photostimulated Oxygen Exchange and Photochemical Properties of Uranyl Ions. *Inorg. Chem. Acta* **1987**, *139* (1), 345–351. https://doi.org/10.1016/S0020-1693(00)84116-X.
(29) Gorman-Lewis, D.; Fein, J. B.; Burns, P. C.; Szymanowski, J. E. S.; Converse, J. Solubility Measurements of the Uranyl Oxide Hydrate Phases Metaschoepite, Compreignacite, Na–Compreignacite, Becquerelite, and Clarkeite. *J. Chem. Thermodyn.* **2008**, *40* (6), 980–990. https://doi.org/10.1016/j.jct.2008.02.006.
(30) Sonneveld, E. J.; Visser, J. W. Automatic Collection of Powder Data from Photographs. *J Appl Crystallogr* **1975**, *8* (1), 1–7. https://doi.org/10.1107/S0021889875009417.
(31) *MATLAB*, 9.9.0.1570001 (R2020b) Update 4.; The MathWorks Inc.: Natick, Massachusetts, 2020.

(32) Ilavsky, J.; Jemian, P. R. Irena: Tool Suite for Modeling and Analysis of Small-Angle Scattering. *J Appl Cryst* **2009**, *42* (2), 347–353. https://doi.org/10.1107/S0021889809002222.
(33) Tiede, D. M.; Mardis, K. L.; Zuo, X. X-Ray Scattering Combined with Coordinate-Based Analyses for Applications in Natural and Artificial Photosynthesis. *Photosynth Res* **2009**, *102* (2), 267–279. https://doi.org/10.1007/s11120-009-9475-6.
(34) McGrail, B. T.; Sigmon, G. E.; Jouffret, L. J.; Andrews, C. R.; Burns, P. C. Raman Spectroscopic and ESI-MS Characterization of Uranyl Peroxide Cage Clusters. *Inorg. Chem.* **2014**, *53* (3), 1562–1569. https://doi.org/10.1021/ic402570b.
(35) Alcock, N. W. The Crystal and Molecular Structure of Sodium Uranyl Triperoxide. *J. Chem. Soc. A* **1968**, *0* (0), 1588–1594. https://doi.org/10.1039/J19680001588.
(36) Dembowski, M.; Bernales, V.; Qiu, J.; Hickam, S.; Gaspar, G.; Gagliardi, L.; Burns, P. C. Computationally-Guided Assignment of Unexpected Signals in the Raman Spectra of Uranyl Triperoxide Complexes. *Inorg. Chem.* **2017**, *56* (3), 1574–1580. https://doi.org/10.1021/acs.inorgchem.6b02666.
(37) Clark, D. L.; Conradson, S. D.; Donohoe, R. J.; Keogh, D. W.; Morris, D. E.; Palmer, P. D.; Rogers, R. D.; Tait, C. D. Chemical Speciation of the Uranyl Ion under Highly Alkaline Conditions. Synthesis, Structures, and Oxo Ligand Exchange Dynamics. *Inorg. Chem.* **1999**, *38* (7), 1456–1466. https://doi.org/10.1021/ic981137h.
(38) Sarrasin, L.; Miro, S.; Jégou, C.; Tribet, M.; Broudic, V.; Marques, C.; Peuget, S. Studtite Formation Assessed by Raman Spectroscopy and 18O Isotopic Labeling during the Oxidative Dissolution of a MOX Fuel. *J. Phys. Chem. C* **2021**, acs.jpcc.1c04392. https://doi.org/10.1021/acs.jpcc.1c04392.
(39) Miró, P.; Vlaisavljevich, B.; Gil, A.; Burns, P. C.; Nyman, M.; Bo, C. Self-Assembly of Uranyl-Peroxide Nanocapsules in Basic Peroxidic Environments. *Chem. Eur. J.* **2016**, *22* (25), 8571–8578. https://doi.org/10.1002/chem.201600390.
(40) Miró, P.; Pierrefixe, S.; Gicquel, M.; Gil, A.; Bo, C. On the Origin of the Cation Templated Self-Assembly of Uranyl-Peroxide Nanoclusters. *J. Am. Chem. Soc.* **2010**, *132* (50), 17787–17794. https://doi.org/10.1021/ja1053175.
(41) Lin, C.-J. Projected Gradient Methods for Nonnegative Matrix Factorization. *Neural Computation* **2007**, *19* (10), 2756–2779. https://doi.org/10.1162/neco.2007.19.10.2756.
(42) Woods, R. J.; Spinks, J. W. T. *An Introduction to Radiation Chemistry*, 3rd ed.; New York : Wiley, 1990.
(43) Traustason, H.; Aksenov, S. M.; Burns, P. C. The Lithium–Water Configuration Encapsulated by Uranyl Peroxide Cage Cluster $U_{24}$. *Cryst. Eng. Comm.* **2019**, *21* (3), 390–393. https://doi.org/10.1039/C8CE01774C.
(44) Lussier, A. J.; Lopez, R. A. K.; Burns, P. C. A Revised and Expanded Structure Hierarchy of Natural and Synthetic Hexavalent Uranium Compounds. *Can. Mineral.* **2016**, *54* (1), 177–283. https://doi.org/10.3749/canmin.1500078.
(45) Burns, P. C. Hydrated Uranium Oxides. In *Reference Module in Materials Science and Materials Engineering*; Elsevier, 2020; pp 557–577. https://doi.org/10.1016/B978-0-12-803581-8.11633-9.
(46) Hawthorne, F. C.; Finch, R. J.; Ewing, R. C. Schoepite and Dehydrated Schoepite. *MRS Proc.* **1995**, *412*, 361. https://doi.org/10.1557/PROC-412-361.

(47) Plášil, J. Uranyl-Oxide Hydroxy-Hydrate Minerals: Their Structural Complexity and Evolution Trends. *Eur. J. Mineral.* **2018**, *30* (2), 237–251. https://doi.org/10.1127/ejm/2017/0029-2690.

For Table of Contents Only

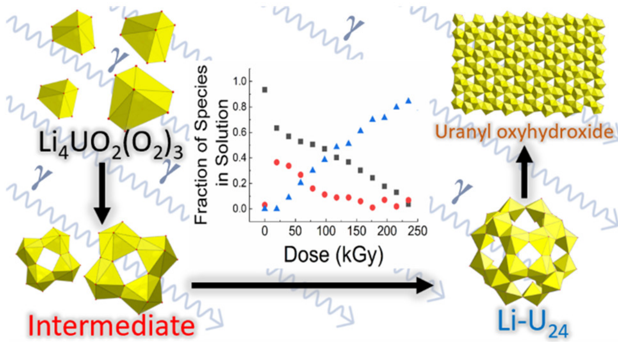


*TOC Graphic:* Polyhedral representations of lithium uranyl triperoxide convert to uranyl peroxide tetramers which then assemble into the lithium uranyl peroxide cage cluster $U_{24}$. The graph in the middle shows the relative concentration of each of these species in solution as a function of dose. Finally, $U_{24}$ precipitates to form a uranyl oxyhydroxide sheet structure. This is all induced by gamma radiation which is shown in the background.